GPS measurements of near-field deformation along the southern Dead Sea Fault System

Eid Al Tarazi, Jafar Abu Rajab, Francisco Gomez, William Cochran, Rani Jaafar, Matthieu Ferry

Geochemistry Geophysics Geosystems G3

Article
Volume 12, Number 12
29 December 2011
Q12021, doi:10.1029/2011GC003736
ISSN: 1525-2027

Published by AGU and the Geochemical Society

GPS measurements of near-field deformation along the southern Dead Sea Fault System

Eid al Tarazi and Jafar Abu Rajab
Faculty of Natural Resources and Environment, Department of Earth and Environmental Sciences, Hashemite University, 13115 Zarqa, Jordan

Francisco Gomez, William Cochran, and Rani Jaafar
Department of Geological Sciences, University of Missouri, Columbia, Missouri 65211, USA (fgomez@missouri.edu)

Matthieu Ferry
Geosciences Laboratory, University Montpellier 2, F-34095 Montpellier, France

[1] Analysis of short-term deformation along the southern part of Dead Sea Fault (DSF) provides a systematic view of kinematics this part of the continental transform. The southern DSF consists of two principal segments: the Wadi Araba and Jordan Valley faults. In addition to other regional continuous GPS data, this study uses new data from 25 survey sites and 4 continuous GPS stations in Jordan for improved near-field observations. Resulting velocities are reported with 1-σ uncertainties ranging from 0.4–1.0 mm/yr. Application of elastic dislocation models yields estimates of slip rates for Wadi Araba and Jordan Valley faults are 4.9 ± 0.4 mm/yr and 4.7 ± 0.4 mm/yr, respectively. Modeling also suggests different depths of effective fault locking with 15 ± 5 km and 8 ± 5 km for the Wadi Araba and Jordan Valley faults, respectively. These slip rates are generally consistent with the upper end of the range of slip rates estimated from late Quaternary geology. Spatial variations in effective fault locking generally correspond with a heterogeneous mantle lithosphere. A similar observation can be observed along the southern San Andreas Fault, and this may reflect the influence of heterogeneity in the uppermost mantle on crustal faulting processes.

Components: 10,000 words, 6 figures, 2 tables.

Keywords: Dead Sea Fault; Global Positioning System; Jordan.

Index Terms: 1209 Geodesy and Gravity: Tectonic deformation (6924); 8002 Structural Geology: Continental neotectonics (8107); 8111 Tectonophysics: Continental tectonics: strike-slip and transform.

Received 2 June 2011; **Revised** 14 November 2011; **Accepted** 14 November 2011; **Published** 29 December 2011.

al Tarazi, E., J. Abu Rajab, F. Gomez, W. Cochran, R. Jaafar, and M. Ferry (2011), GPS measurements of near-field deformation along the southern Dead Sea Fault System, *Geochem. Geophys. Geosyst.*, *12*, Q12021, doi:10.1029/2011GC003736.

1. Introduction

[2] The Dead Sea Fault (DSF) is the left-lateral, continental transform bounding the northwestern Arabian plate and the Sinai plate in the eastern Mediterranean region. Compared with other continental transforms, the relatively simple structure of DSF is appealing for elucidating fundamental insight on the kinematics of large strike-slip faults. Additionally, documenting strain accumulation is

also important for assessing the regional earthquake hazard.

[3] Regional plate models for the eastern Mediterranean region provide first-order constraints on rates of fault slip associated with plate boundaries. Although plate motion is a fundamental constraint for fault slip, slip rates predicted by such models are dependent upon the assumed fault geometries of the corresponding plate boundaries. Furthermore, such models are generally insufficient for directly assessing spatial variations in fault kinematics that may reflect more localized aspects of continental deformation.

[4] Neotectonic slip rate estimates, on the other hand, provide direct observations of fault kinematics. However, direct comparisons of neotectonic slip rates can often be complicated by epistemic uncertainties specific to each study site. In contrast to ad hoc comparison of point measurements corresponding with geologic (i.e., neotectonic) estimates of slip rate, near-field geodetic networks permit assessing spatial kinematic variations from a self-consistent perspective. More specifically, measurement and model-based assumptions will be identical and systematic, so that spatial variability may be more confidently assessed.

[5] This study assesses the kinematics of the southern DSF using new, high-precision Global Positioning System (GPS) measurements. These results complement other recent studies of near-field deformation along the northern DSF [*Alchalbi et al.*, 2010] and central DSF [*Gomez et al.*, 2007], and they build upon previous studies of near-field deformation that were limited only to parts of the southern DSF [e.g., *Wdowinski et al.*, 2004; *Le Beon et al.*, 2008]. Kinematic modeling of GPS velocities suggests along-strike variations in patterns of strain accumulation that correspond with seismogenic fault segmentation and lithospheric properties. Similar patterns are also observed along the southern San Andreas Fault, and these may reflect the influence of a heterogeneous mantle lid on crustal faulting processes.

2. Active Tectonic Setting

[6] The N-S striking Dead Sea Fault (DSF) spans nearly 900 km, linking proto-oceanic spreading in the Red Sea with continental escape tectonics of the Anatolian plate. The DSF accommodates the left-lateral motion of Arabian plate relative to the Sinai plate as they converge with Eurasia and Anatolia and consists of three main sections (Figure 1): (1) A southern section spanning from the Gulf of Aqaba through the Jordan Valley, (2) A NNE-SSW striking restraining bend through the Mount Lebanon and Anti Lebanon ranges, and (3) A northern section tracing along the Syrian Coastal Mountains until it intersects the East Anatolian Fault in southern Turkey. The southern section of the DSF, the focus of this study, is approximately 350 km in length and consists of two major segments: The Wadi Araba Fault (WAF) and the Jordan Valley Fault (JVF), which bound the Dead Sea pull-apart basin.

[7] Total left-lateral slip of 105 km is observed along the southern DSF [*Freund et al.*, 1970]. Left-lateral slip along the southern DSF initiated around 17–18 Ma [*Garfunkel and Ben-Avraham*, 2001] and accrued 60 km of displacement during a first phase of motion [e.g., *Bartov et al.*, 1980, *Freund et al.*, 1970]. A second phase of movement started during the late Miocene or early Pliocene [*Quennell*, 1984] and appears to correspond with the onset of oceanic spreading in the Red Sea [e.g., *Hempton*, 1987]. Total displacements on the southern and northern sections of the DSF during this episode are 45 km and 20–25 km, respectively [*Freund et al.*, 1970; *Quennell*, 1984]; the difference may be accommodated by up to 20 km of shortening of the Palmyride fold belt [e.g., *Chaimov et al.*, 1990]. Some studies suggest that, during the late Cenozoic, the DSF may have developed a regional trans-tensional component of motion (i.e., a "leaky" transform) which is thought to be partly responsible for the opening of the Dead Sea basin [*Garfunkel*, 1981; *Freund et al.*, 1970]. Despite this transtension, crustal thickness varies smoothly across the southern DSF and may connect to a lower crustal detachment [*Weber et al.*, 2009]. Modest seismic activity also suggests that the NW-SE striking Carmel Fault (Figure 1) may transfer some motion off of the main structure of the DSF [e.g., *Hofstetter et al.*, 1996].

[8] In addition to transform motion, late Cenozoic mafic volcanic activity has occurred in the Arabian plate adjacent to the DSF. Cenozoic volcanism occurs in three regions [e.g., *Barberi et al.*, 1980]: (1) Within the Dead Sea/Jordan Valley rift zone, (2) Along the eastern margin of the rift, and (3) in the Harrat Al Sham in northern and eastern Jordan [e.g., *Ilani et al.*, 2001; *Garfunkel*, 1989; *Camp and Roobol*, 1989]. Mafic volcanism initiated around 13 Ma and shows geochemical signatures of a mixed asthenospheric and lithospheric source [*Shaw et al.*, 2003].

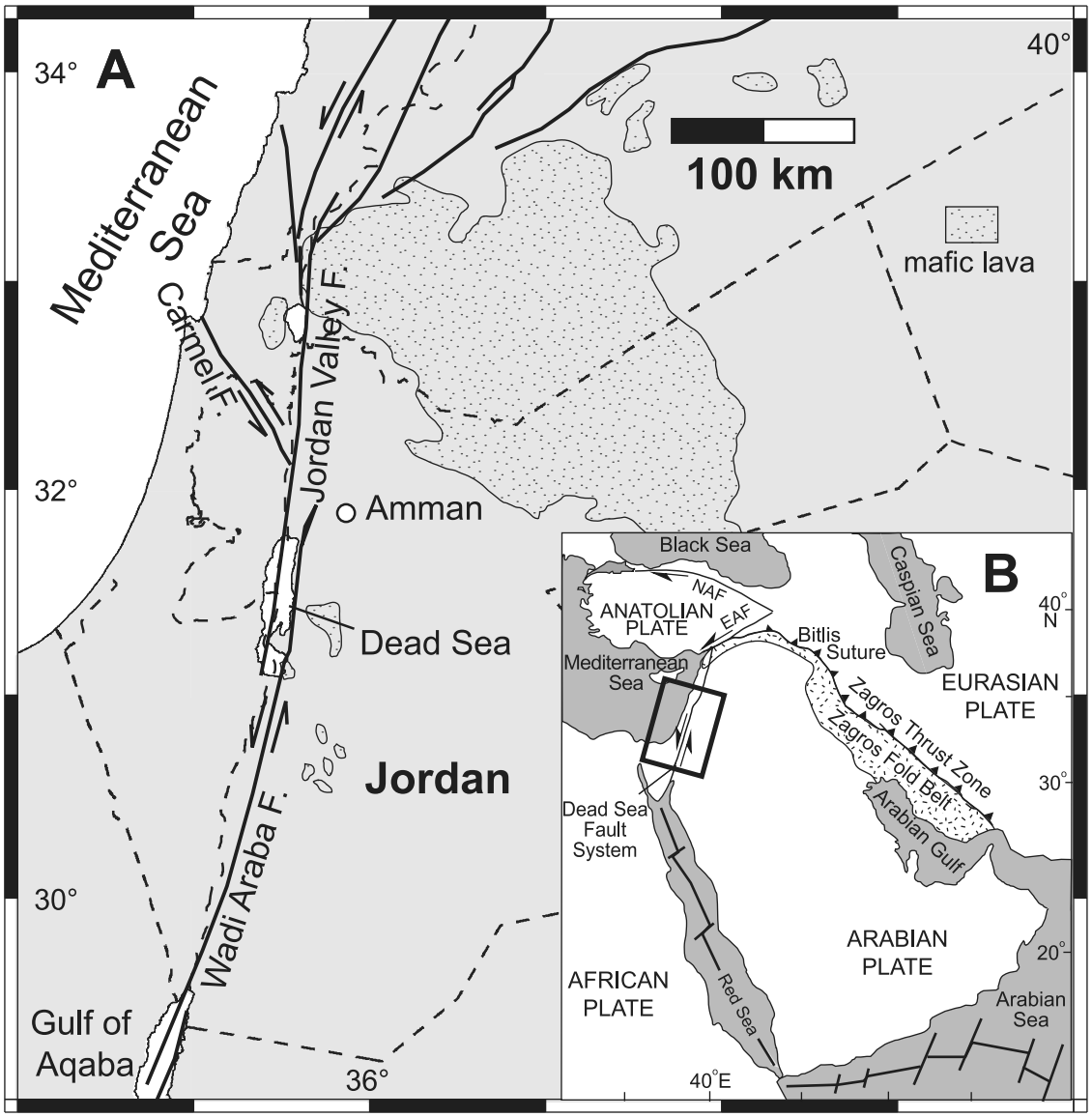

Figure 1. (a) Regional tectonic map of the Dead Sea Fault System. (b) Inset shows the broader setting of the Arabian plate.

[9] Seismological analyses of the mantle lithosphere beneath the southern Dead Sea Fault suggest differences in the nature of the mantle lid between the Wadi Araba and Jordan Valley. Pn velocity tomography [*Al-Lazki et al.*, 2004], Pg Attenuation [*Bao et al.*, 2011], and Sn attenuation [*Al-Damegh et al.*, 2004] are consistent in suggesting normal, but thin, lithosphere beneath the Wadi Araba versus highly attenuating and slower mantle lithosphere beneath the Jordan Valley (as well as northern Jordan, and southwestern Syria). The Wadi Araba region was also studied by *Laske et al.* [2008] using surface wave analysis to estimate a thin mantle lid (80-km thickness) of normal S wave velocity. At lower spatial resolution, *Chang and Van der Lee* [2011] document the restricted nature of the mantle S wave anomaly and suggest it as evidence of a plume beneath NW Arabia.

[10] Historical records document the strong earthquake potential of the southern DSF, despite a general seismic quiescence during the past century [e.g., *Ambraseys et al.*, 1994]. Aside from a large earthquake in the Gulf of Aqaba in 1995 (M ~7.4), the southern DSF has not experienced large, surface-rupturing earthquakes along the WAF and JVF since 1458 AD and 1033 AD, respectively [e.g., *Klinger et al.*, 2000b; *Ferry et al.*, 2011]. On the other hand, recent moderate earthquakes, such as the 2004 (M~5.3) earthquake near the northern

end of the Dead Sea basin [*Al-Tarazi et al.*, 2006; *Lazar et al.*, 2006] attest to the present-day activity of the transform, and paleoseismic studies suggest return periods of large earthquakes average ~1,100 years over the past 14 k.y. [e.g., *Ferry et al.*, 2011], although temporal clustering of earthquakes over longer time periods may also occur [e.g., *Marco et al.*, 1996]. Distributions of historical macroseismic observations also suggest general seismogenic segmentation between the Jordan Valley and the Wadi Araba for the largest earthquakes [e.g., *Ferry et al.*, 2011]. The boundary between these segments is generally interpreted to correspond with the Dead Sea basin.

[11] Plate tectonic models predict present-day left-lateral slip rates of 4–8 mm/yr along the DSF [e.g., *Reilinger et al.*, 2006; *McClusky et al.*, 2003; *Joffe and Garfunkel*, 1987; *DeMets et al.*, 1994; *Westaway*, 1994]. However, such fault kinematic predictions are dependent upon the assumed geometry and assume no permanent deformation off of the main faults comprising plate boundaries. Geological estimates of rates for the Wadi Araba Fault during late Pleistocene to Holocene range 2–6 mm/yr [e.g., *Le Beon et al.*, 2010; *Makovsky et al.*, 2008; *Niemi et al.*, 2001; *Klinger et al.*, 2000a; *Ginat et al.*, 1998]. In the Jordan Valley, offset Late Quaternary offset Gullies suggest a slip rate to about 4.7–5.1 mm/yr [*Ferry et al.*, 2007].

[12] Regional, continuous GPS data and elastic dislocation models have been used to propose slip rates of 3.3 ± 4 mm/yr [*Wdowinski et al.*, 2004; *Mahmoud et al.*, 2005] along the southern DSF. However, data for these studies was almost exclusively confined to observations from the Sinai plate. Along the Wadi Araba Fault, detailed near-field GPS measurements and 1-D elastic dislocation models suggest a slip rate of 4.9 ± 1.4 mm/yr [*Le Beon et al.*, 2008]. This work improves upon these geodesy-based kinematic parameters sufficient to assess spatial variations along the entire southern DSF.

3. GPS Measurements

[13] The GPS network used in this study was established in Jordan in 2005 and consists of 29 Survey-Mode sites and four continuous GPS station, as well as other regional continuous GPS stations with publicly available data. Survey-mode GPS sites consist of 10 cm steel pins cemented into bedrock. Most of these sites have been observed annually between 2005 and 2010 (Table 1). GPS antenna were set up using fixed-height antenna masts, and sites were observed for a minimum of 24 h during each survey campaign using Trimble R7 dual-frequency GPS receivers with Trimble Zephyr geodetic antennae. Continuous GPS stations in Jordan used in this study have time series spanning 2–5 years (Table 1).

3.1. Data Processing

[14] Raw GPS data were processed following a standard, two-step procedure using the GAMIT/GLOBK software [*Herring et al.*, 1997; *Dong et al.*, 1998; *King and Bock*, 1998]. In the first step, loosely constrained estimates of station coordinates, orbital and Earth orientation parameters, and atmospheric zenith delays were determined from raw GPS observables using GAMIT. Data from the Jordanian GPS network were analyzed along with raw GPS data from other continuously operating GPS (CGPS) stations in the region. Data from survey campaigns were subdivided into 8–10 h epochs (typically at 2400 UTC), so that multiple, loosely constrained solutions were available for each site during each given campaign. In addition to the times of the four survey campaigns in Jordan, CGPS data, when available, were also analyzed monthly between 2005 and 2009; a summary of the CGPS stations and their observations epochs is provided in Table 1.

[15] Subsequently, a global Kalman filter (GLOBK) was applied to the loosely constrained solutions and their associated covariance matrices in order to estimate a self-consistent set of station coordinates and velocities. As part of this second step, the data were combined with loosely constrained solutions for stations from the International GNSS Service (IGS) processed and distributed by MIT. A six-parameter Helmert transformation was estimated by minimizing the horizontal velocities of 134 globally distributed IGS stations with respect to the 2005 realization of the International Terrestrial Reference Frame (ITRF2005). The WRMS of the residual velocities for the IGS stations into ITRF 2005 was 0.7 mm/yr. During this process, obvious outliers in the continuous and campaign time series for regional sites were identified and removed; data from individual survey campaigns were then amalgamated into single epochs for final velocity estimation.

[16] Accurate characterization of the uncertainties in the velocities is critical to avoid over interpretation of the small tectonic signal associated with the DSF. It is well regarded that the formal, standard

Table 1. Velocities for GPS Sites Shown in Figure 2[a]

Site	Longitude	Latitude	Ve (ITRF)	Vn (ITRF)	Ve (Ar)	Vn (Ar)	Sig. E	Sig. N	Corr.	First (Date)	Last (Date)	Span (yr)
					Jordan							
AQBA	35.018	29.528	21.86	19.72	−1.43	−1.58	0.68	0.68	−0.021	2005.6	2010.5	4.9
ASGF	37.648	32.333	23.10	22.33	0.43	−0.14	0.61	0.62	0.006	2005.6	2010.5	4.9
BISH	36.818	32.156	21.91	20.96	−0.73	−1.15	0.57	0.57	0.003	2005.6	2010.5	4.9
DANA	35.580	30.698	24.68	20.49	1.17	−1.07	0.75	0.71	0.000	2006.5	2010.5	4.0
DASK	35.691	32.501	21.71	20.84	−0.43	−0.76	0.67	0.68	0.005	2005.6	2010.5	4.9
DBUS	35.659	30.897	23.10	20.30	−0.27	−1.29	1.25	1.24	−0.011	2008.5	2010.5	2.0
DRAA	35.572	31.249	21.53	20.39	−1.05	−1.16	0.62	0.62	0.007	2005.6	2010.5	4.9
FIFA	35.456	30.907	21.24	19.56	−2.08	−1.94	1.03	1.06	−0.068	2007.5	2010.5	3.0
HUG1	36.189	32.107	21.51	21.83	−1.04	0.00	0.66	0.67	−0.022	2005.5	2010.5	5.0
HUGS[b]	36.189	32.101	22.26	21.45	−0.29	−0.38	0.45	0.45	0.000	2005.5	2011.0	5.5
JAFR	36.368	30.680	23.40	21.65	−0.27	−0.26	0.67	0.67	0.006	2005.6	2010.5	4.9
JASH	35.915	32.294	21.59	22.19	−0.76	0.49	0.61	0.62	0.012	2005.6	2010.5	4.9
JUST[b]	35.987	32.493	21.41	21.03	−0.80	−0.71	0.70	0.69	−0.001	2008.4	2011.0	2.5
MUD2	35.632	32.158	23.04	19.92	0.65	−1.66	0.67	0.66	0.009	2005.6	2010.5	4.9
MUTA[b]	35.718	31.095	21.90	20.56	−1.33	−1.06	0.56	0.56	−0.001	2007.2	2011.0	3.7
NAML	35.403	30.469	23.53	21.61	−0.12	0.13	1.20	1.21	−0.024	2008.5	2010.5	2.0
NAQB	35.433	30.086	22.28	20.73	−1.67	−0.76	1.84	1.89	0.087	2008.5	2010.5	2.0
NEBO	35.739	31.766	20.53	21.55	−1.19	−0.08	0.94	0.92	0.021	2005.6	2010.5	4.9
PANO	35.602	31.644	21.72	19.27	−1.07	−2.29	1.24	1.25	−0.026	2008.5	2010.5	2.0
PETA[b]	35.469	30.327	22.51	19.78	−1.26	−1.73	0.67	0.67	−0.002	2008.2	2011.0	2.8
PETH	35.455	30.265	23.20	20.54	−0.62	−0.96	1.22	1.20	−0.009	2005.6	2007.5	1.9
QIRA	35.403	30.621	21.55	18.74	−1.98	−2.73	1.03	1.00	−0.052	2007.5	2010.5	3.0
QURA	35.340	29.810	23.07	20.00	−1.07	−1.45	0.59	0.59	0.001	2005.6	2010.5	4.9
RAMA	35.151	29.907	22.52	18.60	−1.51	−2.76	0.83	0.82	−0.009	2007.5	2010.5	3.0
RSAS	35.922	31.514	23.13	20.02	0.18	−1.69	0.66	0.64	−0.010	2005.6	2010.5	4.9
RUMM	35.426	29.630	23.87	20.31	−0.42	−1.18	0.83	0.81	0.004	2007.5	2010.5	3.0
SAFI	35.514	31.078	23.29	19.77	0.09	−1.75	1.21	1.22	−0.010	2008.5	2010.5	2.0
TUBA	36.562	31.319	22.47	21.59	−0.76	−0.40	0.63	0.63	0.004	2005.6	2010.5	4.9
WADR	35.359	30.176	23.08	19.70	−0.78	−1.76	1.22	1.20	−0.005	2008.5	2010.5	2.0
					Southern Lebanon and Syria Survey Sites							
ANJR	35.922	33.740	17.83	20.98	−1.02	−2.09	0.53	0.54	−0.024	2002.4	2007.8	5.4
HZRT	35.880	33.859	17.49	21.21	−1.26	−1.84	0.52	0.51	−0.013	2002.4	2007.8	5.4
JZIN	35.579	33.545	17.72	19.74	−1.21	−3.17	0.58	0.59	−0.001	2002.4	2007.8	5.4
JIYE	35.401	33.641	17.24	19.11	−1.57	−3.72	0.66	0.66	−0.022	2002.4	2007.8	5.4
KBDD	38.437	33.571	20.26	25.18	0.71	0.96	0.46	0.45	−0.010	2001.1	2008.7	7.6
MCHK	35.761	33.516	17.88	20.97	−1.11	−2.03	0.49	0.49	−0.004	2002.4	2007.8	5.4
RBDA	35.162	33.149	18.49	18.45	−0.65	−4.27	0.74	0.76	0.025	2002.4	2007.8	5.4
RSHD	36.913	32.702	20.42	24.15	0.55	0.62	0.44	0.43	−0.009	2001.1	2008.7	7.6
TFEL	36.235	33.860	17.47	22.15	−1.36	−1.07	0.53	0.53	−0.010	2002.4	2007.8	5.4
					Other Regional Sites							
ANKR[b]	32.758	39.887	−0.80	9.96	−16.37	−10.29	0.28	0.28	−0.004	2000.9	2011.0	6.0
AREL[b]	35.209	32.102	20.84	18.00	−1.52	−3.39	0.57	0.57	−0.002	2005.2	2008.6	3.4
BAHR[b]	50.608	26.209	29.89	26.98	0.20	−0.52	0.32	0.31	−0.002	2000.9	2008.6	3.6
BSHM[b]	35.023	32.779	22.21	17.57	0.42	−3.73	0.32	0.32	0.000	2000.9	2011.0	6.0
CSAR[b]	34.890	32.488	20.58	17.43	−1.41	−3.81	0.41	0.41	−0.001	2004.4	2011.0	6.0
DRAG[b]	35.392	31.593	21.55	17.73	−1.23	−3.74	0.32	0.32	0.000	2000.9	2011.0	6.0
DSEA[b]	35.369	31.037	22.62	19.00	−0.58	−2.46	0.45	0.45	−0.001	2005.2	2011.0	5.8
ELAT[b]	34.921	29.509	24.36	18.33	0.07	−2.93	0.33	0.33	−0.002	2001.1	2011.0	6.0
ELRO[b]	35.771	33.182	21.59	19.93	−0.04	−1.71	0.33	0.33	0.000	2000.9	2010.6	5.6
GILB[b]	35.416	32.479	20.84	18.14	−1.26	−3.34	0.33	0.33	0.000	2000.9	2011.0	6.0
JSLM[b]	35.202	31.771	21.45	17.17	−1.16	−4.22	0.37	0.37	0.002	2002.3	2011.0	6.0
KABR[b]	35.145	33.023	20.51	17.67	−1.12	−3.69	0.33	0.32	0.000	2000.9	2011.0	6.0
KATZ[b]	35.688	32.995	21.31	19.86	−0.45	−1.74	0.33	0.33	−0.002	2000.9	2011.0	6.0
LAUG[b]	35.674	34.115	19.70	18.92	−1.18	−2.67	0.39	0.39	0.000	2002.8	2010.7	5.7
LHAV[b]	34.866	31.378	21.43	16.40	−1.42	−4.83	0.37	0.37	−0.001	2001.1	2008.9	3.9
MERS[b]	34.256	36.566	12.49	14.23	−6.13	−6.72	0.35	0.35	0.000	2002.4	2011.0	6.0
NICO[b]	33.396	35.141	18.31	13.20	−1.28	−7.35	0.32	0.32	0.000	2000.9	2011.0	6.0
NRIF[b]	35.036	30.038	22.30	18.12	−1.61	−3.19	0.44	0.44	−0.001	2005.2	2011.0	5.8

Table 1. (continued)

Site	Longitude	Latitude	Ve (ITRF)	Vn (ITRF)	Ve (Ar)	Vn (Ar)	Sig. E	Sig. N	Corr.	First (Date)	Last (Date)	Span (yr)
NSSP[b]	44.503	40.226	27.58	14.86	9.28	−10.42	0.33	0.33	0.000	2001.1	2010.5	5.5
RAMO[b]	34.763	30.598	26.54	20.36	−0.36	−3.71	0.78	0.76	−0.001	2000.9	2011.0	6.0
SLOM[b]	34.284	31.228	24.49	14.64	1.64	−6.33	0.51	0.50	−0.001	2004.7	2011.0	6.0
TELA[b]	34.781	32.068	21.92	17.29	−0.38	−3.90	0.33	0.33	−0.001	2000.9	2011.0	6.0
TRAB[b]	39.776	40.995	24.37	10.99	7.98	−12.38	0.38	0.38	0.000	2000.9	2007.9	2.9
UDMC[b]	36.285	33.510	21.12	21.01	−0.36	−0.86	0.35	0.35	0.000	2002.3	2010.9	5.9
YRCM[b]	34.928	30.992	21.53	17.07	−1.63	−4.19	0.48	0.48	−0.002	2005.5	2010.5	5.0
ZECK[b]	41.565	43.788	24.35	9.09	9.71	−15.02	0.32	0.32	0.000	2000.9	2011.0	6.0
Le Beon et al. (Rotated Into Reference Frame of This Study)												
ABK0	35.270	30.280			0.23	−1.71	1.10	1.18	0.012			
AYN0	35.780	30.960			−0.31	0.02	1.10	1.10	0.035			
BUR0	35.640	30.980			−1.41	1.91	1.22	1.28	0.021			
JEM0	35.080	29.750			−0.73	0.78	1.10	1.23	−0.006			
JFR0	36.190	30.260			−0.06	0.14	1.14	1.16	0.092			
MAN0	35.680	30.170			−0.26	0.51	1.11	1.18	0.051			
QUL0	35.510	30.310			0.83	−1.00	1.05	1.12	0.036			
ROM0	35.310	29.700			1.17	−0.61	1.10	1.24	0.020			
SAF0	35.520	31.080			−0.52	−1.40	1.10	1.10	0.019			
SUL0	35.440	30.440			−0.88	0.10	1.16	1.20	0.023			
BOR0	34.610	30.510			−0.69	−3.85	1.08	1.12	−0.042			
DIM0	35.080	31.030			−0.22	−5.02	1.07	1.08	−0.002			
MAP0	34.970	30.320			−1.67	−2.43	1.04	1.12	−0.015			
MNH0	35.130	30.290			0.23	−3.62	1.09	1.16	0.000			
SAG0	34.860	29.780			−0.23	−3.13	1.09	1.22	−0.031			
TAM0	35.300	30.950			0.49	−4.11	1.07	1.08	0.010			
TIM0	34.960	29.780			0.47	−2.93	1.08	1.22	−0.020			

[a]Velocities are presented in ITRF2005 and Arabia-fixed reference frames.
[b]Denotes continuous GPS station.

error of the GPS solution underestimates the true uncertainty in the GPS velocities [e.g., *Zhang et al.*, 1997; *McClusky et al.*, 2000]. Detailed studies of CGPS data indicate that the noise in GPS time series may be characterized by colored noise that varies from fractal white noise to random walk [*Zhang et al.*, 1997; *Mao et al.*, 1999]. However, by estimating relative velocities (i.e., defining "local" plate reference frames), we implicitly remove the common mode component of the noise within the region [*McClusky et al.*, 2000]. The remaining noise error in GPS observations accounts for factors such as monument stability and setup errors. In GPS processing with GLOBK, noise is modeled as a time-dependent, random walk error in the velocity estimation. In our study, we applied a random walk noise of 1.3 mm/sqrt(yr), which represents the average of random walk noise estimated for CGPS sites in the eastern Mediterranean region by *Reilinger et al.* [2006]. We believe this is justified owing to the use of extremely stable, fixed-height antenna masts during the all of the survey campaigns.

[17] After stabilizing the reference frame, the site velocities were resolved to an Arabia-fixed reference frame, which facilitates assessing the local deformation. The reference frame was defined by minimizing the motion of 6 GPS sites distributed around Arabia (Figure 2, inset); the WRMS of the residual velocities used to define the Arabian plate is 0.8 mm/yr. GPS velocities (in ITRF2000-NNR and Arabia-fixed reference frames) for the sites around the southern DSF are provided in Table 2. We estimate ITRF2005 Euler pole for the Arabian plate is 48.790 ± 0.9° N/5.133 ± 1.9° W/0.481 ± 0.019°/Myr. This compares with results of *Reilinger et al.* [2006]. However, the error reported here is larger because Reilinger et al. analyzed longer time series for the regional CGPS sites, whereas our study primarily analyzed data during the time periods of GPS survey campaigns in Jordan (2005–2010).

3.2. Results: Velocity Field

[18] As shown in Figure 2, the velocity field depicts the overall, left-lateral shear along the southern DSF. The overall orientations of velocity vectors are coherent, and the velocity magnitudes demonstrate a gradual decrease toward the DSF. This pattern is consistent with a locked fault that accumulates elastic strain.

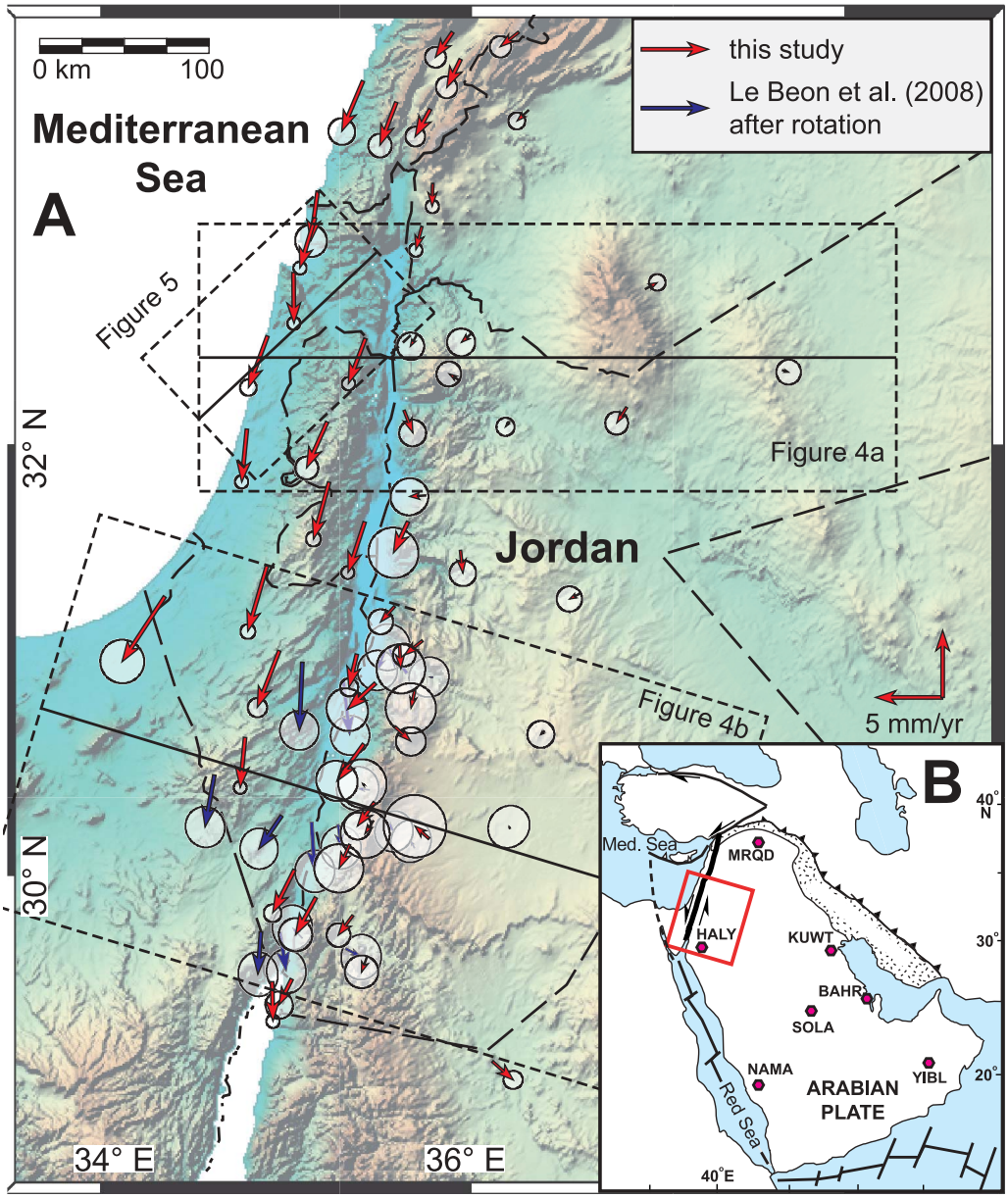

Figure 2. (a) GPS velocities along the southern Dead Sea Fault System. Velocities are shown in an Arabian-fixed reference frame. In addition to velocities from this analysis, velocity vectors reported by *Le Beon et al.* [2008] across the Wadi Araba Fault have been rotated into our reference frame and included for completeness. (b) Map depicting location of GPS sites used to define the Arabian plate reference frame.

[19] To construct a more complete view of near-field deformation, we have also incorporated GPS velocities reported by *Le Beon et al.* [2008] spanning the Wadi Araba. Prior to combining these velocities with results from our analysis, a rotational transformation was estimated that minimized the residual misfit of GPS velocities for 11 sites that are common to Le Beon et al. and this study (Figure 3); the RMS fit was 0.6 mm/yr, much less than the 1-σ uncertainties reported by Le Beon et al. This transformation was applied to velocities reported by Le Beon et al., before incorporating into our analysis; adding these velocities produces a more spatially complete coverage of the southern DSF.

[20] Because transform motion primarily involves strike-slip, an initial assessment of fault kinematics can be made by analyzing GPS velocities along profiles across the fault (Figure 4). Two profiles are examined that cross the WAF and the JVF,

Table 2. Kinematic Results From Block Models for the Southern Dead Sea Fault[a]

	Locking Depth (km)	Slip Rate (mm/yr)
	Jordan Valley Fault	
Minimum	4	4.4
Maximum	13	5.2
Preferred	8	4.7
	Wadi Araba Fault	
Minimum	10	4.6
Maximum	24	5.3
Preferred	15	4.9

[a]Minima and Maxima are based on the probable (1-sigma) confidence region (Figure 6) estimated after modeling 500 iterations of the block model allowing for Gaussian noise of site velocities. Preferred parameters correspond to the minimum WRMS from noise analysis; asymmetry of probability distribution is skewed toward shallower locking depths.

respectively. The profiles in Figure 4 decompose the GPS velocities into motions parallel and perpendicular to the DSF.

[21] In both profiles, the velocities parallel to the transform show a progressive increase in southward velocity from east to west; this pattern is generally consistent with basic models of elastic strain accumulation for strike-slip faults and will be explored further below. GPS velocities perpendicular to the DSF do not depict statistically significant motions indicative of either transtension or transpression.

4. Modeling of GPS Velocities

[22] In this study, quantitative kinematic analysis of these GPS velocities is accomplished using elastic dislocation models. Elastic dislocation models are commonly applied to geodetic data (including GPS) in order to relate point velocities and/or strains to fault kinematic parameters including slip rate and depth of fault locking. As an example of further utility, *Devès et al.* [2011] applied elastic dislocations to explain long-term deformation and first-

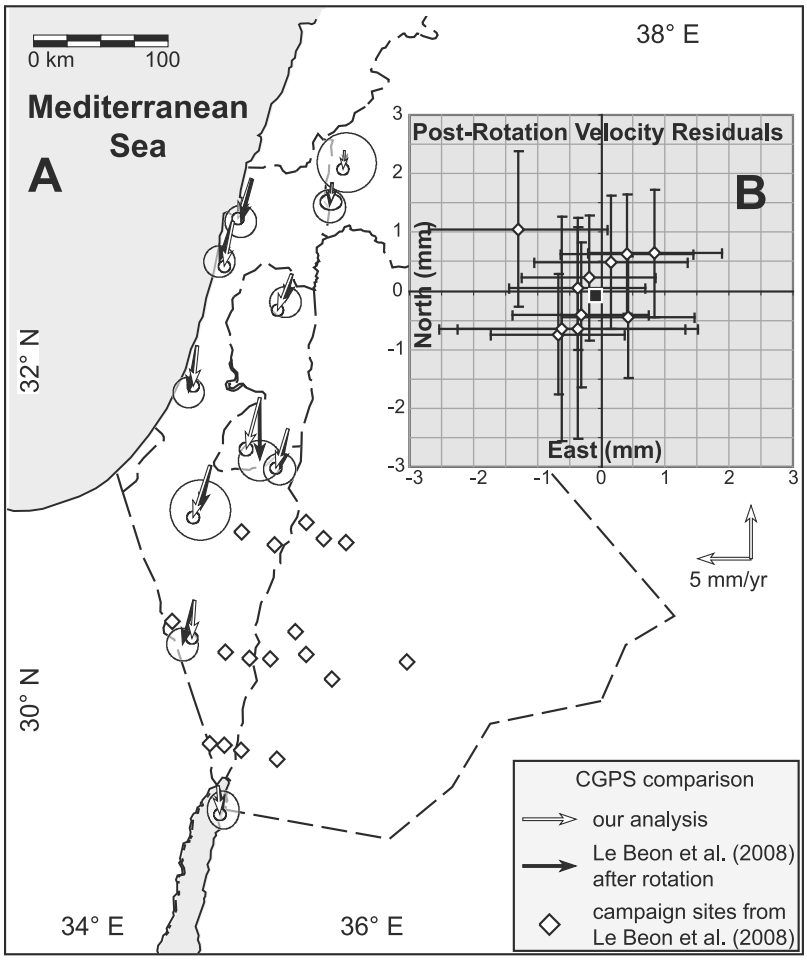

Figure 3. (a) Comparison of GPS velocities for common sites (continuous GPS stations) with results of *Le Beon et al.* [2008]. Velocities of Le Beon et al. (white arrows) are shown after rotation. (b) Scatterplot of residual velocities for common sites after transformation to our reference frame. The mean residual of the fit is 0.4 mm/yr.

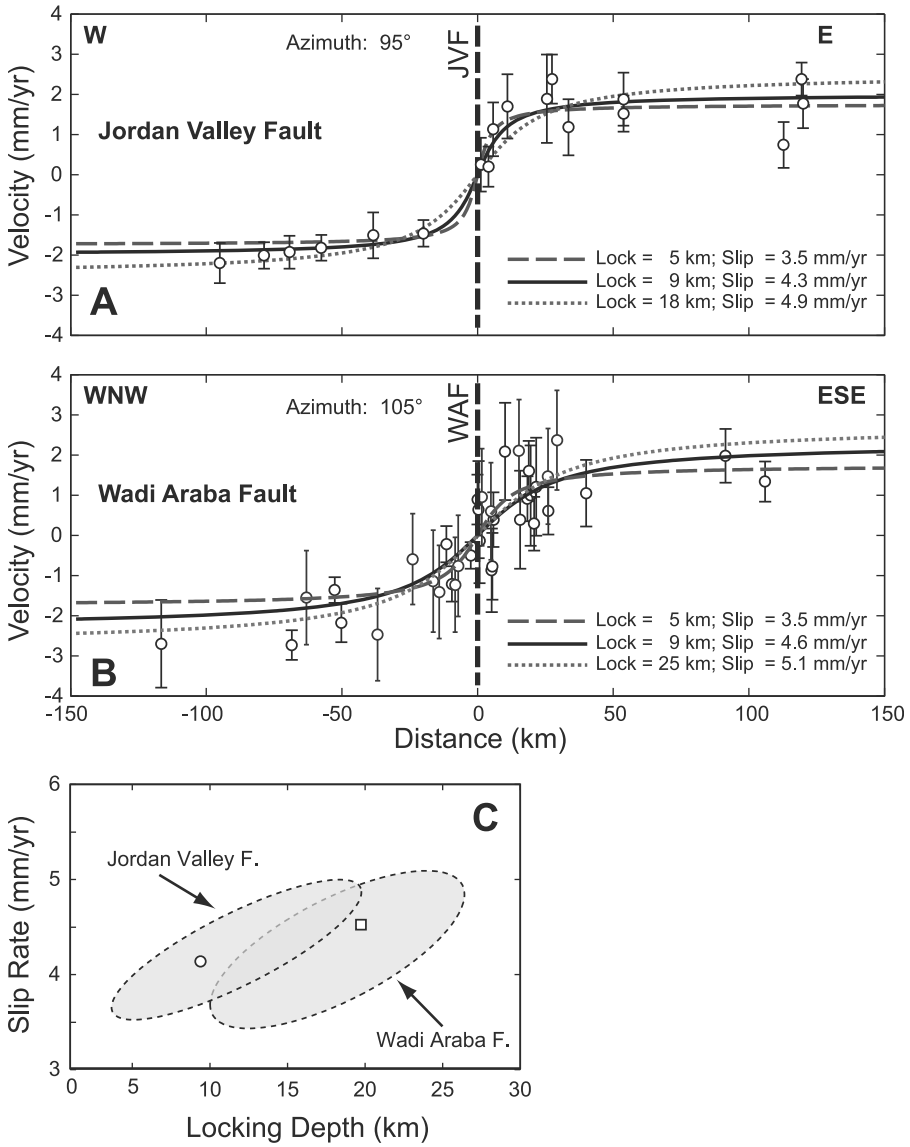

Figure 4. Profiles of strike-parallel GPS velocities across (a) the Jordan Valley and (b) Wadi Araba. For each profile, 1-D elastic dislocation models (discussed in the text) are shown for a range of slip rates and locking depths. Heavy, dashed line denotes the location of the DSF along each profile. See Figure 2 for location. (c) 2-sigma confidence limits on slip rates and locking depths estimated from Monte Carlo simulation of the noise level in the data. Although there is a suggestion of different fault locking depths for the two fault segments, such a distinction is not robust from these 1-D models.

order topography along the southern Dead Sea Fault. Although topography was their primary constraint, Dèves et al. demonstrated overall consistency with previous GPS results [*Le Beon et al.*, 2008]. Hence, improved fault kinematic parameters may help refine models of long-term deformation, too.

[23] In this study, a two-step modeling approach is used: (1) Initially, 1-D profile models are applied separately to the Wadi Araba and Jordan Valley faults to assess kinematic consistency. (2) Subsequently, 2-D elastic block models are applied to address regional tectonic questions and more robustly estimate kinematic parameters. Results from the 1-D models provide justification for the geometry that must be assumed in the 2-D models.

[24] The locking depths modeled here are more properly considered as 'effective' locking depths, as the actual variation of slip with depth is more likely gradual, rather than abrupt. However, geodetic measurements cannot unambiguously resolve the depth distribution of slip [e.g., *Savage*, 2006].

However, the effective locking depth can be considered as a description of the degree to which a crustal fault accumulates earthquake moment [e.g., *Smith-Konter et al.*, 2011].

4.1. 1-D Elastic Dislocation Models and Consistency of Wadi Araba and Jordan Valley Faults

[25] A preliminary estimate of the slip rates may be provided by applying 1-dimensional (i.e., profile) elastic dislocation models using the analytical function presented by *Savage and Burford* [1973]. Although very simplified, this approach permits comparing independent models for the Wadi Araba and Jordan Valley faults (in block modeling discussed below, they are implicitly linked).

[26] In this 1-D analysis, theoretical station velocity relative to the fault (v) is maintained by fitting GPS data to a locked fault model depth (D) as a function of long-term slip rate (b) and horizontal distance (x) from fault:

$$v = (b/\pi)\tan^{-1}(x/D) \quad (1)$$

The long-term slip rate, b, corresponds with the loading of the locked, upper portion of the fault by stable sliding in the lower crust.

[27] Best fit 1-D models were estimated using a grid search inversion. The inverse modeling solved for three parameters: slip rate, locking depth, and a constant that minimizes velocity at the fault. The constant term changes the reference frame to that of the fault (rather than one plate or the other), as required by the analytical solution in equation (1). Uncertainties for 1-D model parameters were estimated using a 'Monte Carlo' simulation of assumed, Gaussian noise in the velocity data [e.g., *Gomez et al.*, 2007]; the inversion was repeated allowing velocities to vary with a normal probability based on the standard deviation reported by GLOBK. In total, 1,000 iterations were performed for each profile, and the probable (1-sigma) uncertainty was estimated from the scatter the resulting parameters.

[28] As shown in Figure 4, the Jordan Valley and Wadi Araba profiles are statistically similar, with fault slip rates and locking depths ranging from 4.5–5.1 mm/yr. Initial estimates of locking depths are 5–18 km for the Jordan Valley Fault and 10–25 km for the Wadi Araba Fault. Preferred estimates of 1-D model slip rates and locking depths are based on the minimum WRMS from the inversions: 4.2 mm/yr at 9 km for the JVF, and 4.5 at 19 km for the WAF. The main implication of this initial analysis is that slip rates of the JVF and WAF are statistically similar, although locking depths may vary. For the tectonics of the Dead Sea basin, this implies that slip across the step-over is generally conserved between its two bounding faults. Therefore, extension within the basin is primarily a result of the displacement gradient resulting from the transfer of slip from the WAF to the JVF.

[29] From these profiles, there does not appear to be a significant transfer of slip from the DSF to the Carmel Fault at the present time. This is also suggested from the velocities of continuous GPS sites in a profile spanning the Carmel Fault (Figure 5), which show no statistically significant changes in motion perpendicular to the fault, nor along strike. The continuous GPS stations spanning the Carmel Fault have velocity uncertainties less than 0.5 mm/yr (1 sigma) (Figure 5). Our results reaffirm and refine earlier interpretations of the Carmel Fault from GPS [*Wdowinski et al.*, 2004; *Le Beon et al.*, 2008] and InSAR analyses [*Nof et al.*, 2007] and further reduce the uncertainty and maximum slip rate constraint. Our results disagree with recent interpretations of 4.5 mm/yr of right-lateral displacement by *Reinking et al.* [2011] based on short occupation (typically less than 6 h), survey-mode GPS data. However, we believe the CGPS results are more reliable than the survey-mode results of *Reinking et al.* [2011], owing to survey epochs of longer duration (typically 24-h) and greater number (in this study, weekly observations spanning 6+ years). Hence, we interpret that the Carmel Fault slips at a rate less than 0.5 mm/yr, at most.

[30] These 1-D models provide preliminary kinematic parameters. The uncertainties are relatively large, but comparable to those reported from similar models by *Le Beon et al.* [2008]. On the other hand, such models are limited in that they are incapable of accounting for oblique plate motion, which is important for testing the hypothesis of a "leaky" transform along the southern DSF. These 1-D models are analyzed independently of on another. The confidence limits on locking depths and slip rates shown in Figure 4c are large and demonstrate considerable overlap, although optimal solutions suggest different depths of fault locking, the distinction is not robust from the 1-D models, alone. However, since they are part of the same plate boundary, fault slip rates must be consistent and compatible with plate motion, and this provides additional constraints that may reduce parameter uncertainties.

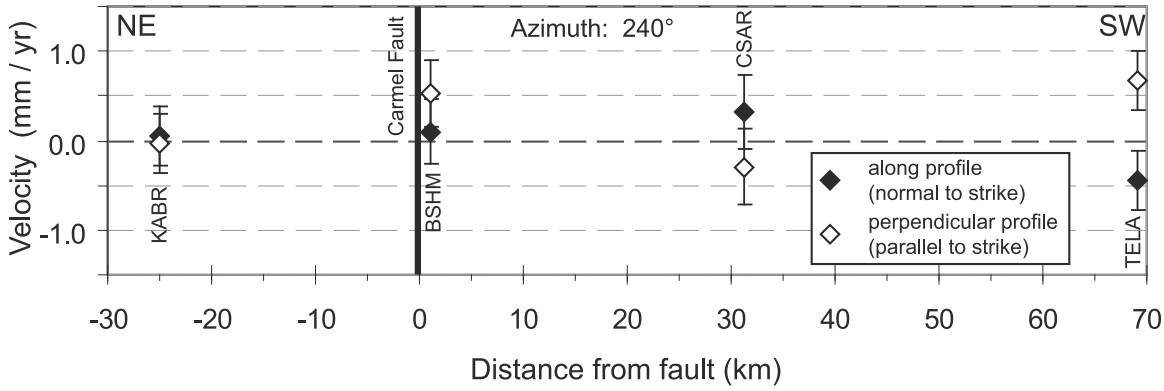

Figure 5. Profile of velocities perpendicular and parallel to the Carmel Fault. The four continuous GPS stations shown were selected owing to their similar (and maximum) distance away from the main Dead Sea Fault in order to minimize differences in velocities resulting from locking and elastic strains associated with the main transform. See Figure 2 for location.

4.2. 2-D Elastic Block Modeling

[31] A more geometrically appropriate elastic model (and more robust estimate of the fault slip rate) involves 2-D blocks bounded by faults of finite lengths, rather than 1-D profiles across faults of infinite length. This modeling follows the methodology of *Meade and Loveless* [2009] and considers the spatial variations in the velocity field due to fault geometry and the effect of block rotations that are not accounted for in 1-D models. In this approach, an optimal fit between plate motion, fault slip, and GPS velocities is determined using a linearized least squares inverse method. Once again, the motivation is that rigid plate motion can provide an additional constraint to reduce uncertainties in the modeled fault parameters.

[32] In this block model, far-field velocities within Arabia are used (the same ones used in the Arabian-plate definition). Sites in Lebanon [*Gomez et al.*, 2007] were included, as well. GPS near-field, survey-sites from Syria were not used in the modeling, owing to concerns of internal deformation of both northern Arabia and the northern Sinai plates [*Alchalbi et al.*, 2010]. Data were weighted based on the velocity uncertainties and spatial density of survey sites. The block model for the southern DSF is a relatively simple, vertical fault that steps leftward at the Dead Sea basin (Figure 5). Owing to the statistical similarity of slip rates in the 1-D models (above), the fault geometry was approximated with a step-over at the Dead Sea basin, and the Carmel fault was not included.

[33] Our analysis estimated locking depth by with multiple runs of the block modeling code; for each run, locking depth was varied by 1 km increments between 1 km and 35 km, and the optimal combination of locking depths and slip rates were determined based on minimizing the weighted RMS of the residual, near-field velocities. In order to quantify uncertainties for the model parameters, these models were run with Gaussian noise added to each velocity. Based on the scatter of the optimal parameters for more than 2,000 model iterations, confidence limits (ellipses on scatterplots) were estimated for locking depths (Figure 6b) and slip rates (Figure 6c). Kinematic parameters predicted by the block model for the Wadi Araba and Jordan Valley faults are shown in Table 2.

[34] The confidence limits on effective locking depths (Figure 6b) suggest different locking depths for the two main branches of the southern DSF. This is demonstrated by the confidence regions, which are generally located outside the region of equal locking depth (dashed gray line in Figure 6b). As shown in Figure 6b, the distinction is generally supported at the 90% confidence level, although the 95% confidence ellipse does not completely exclude the possibility. Hence, at the 90% confidence level, the effective locking depth on the JVF is shallower than the effective locking depth on the WAF; the robustness of this distinction is derived from the plate motion constraint in the block modeling method.

[35] The 95% confidence ellipse for slip rates in Figure 6c demonstrates high covariance between the Wadi Araba and Jordan Valley faults. This is reflects the fact that both slip rates linked through their mutual dependency on the Arabia-Sinai Euler pole. Owing to the Euler pole's position relative to the southern DSF, predicted slip rates are slightly lower on the Jordan Valley Fault than along the

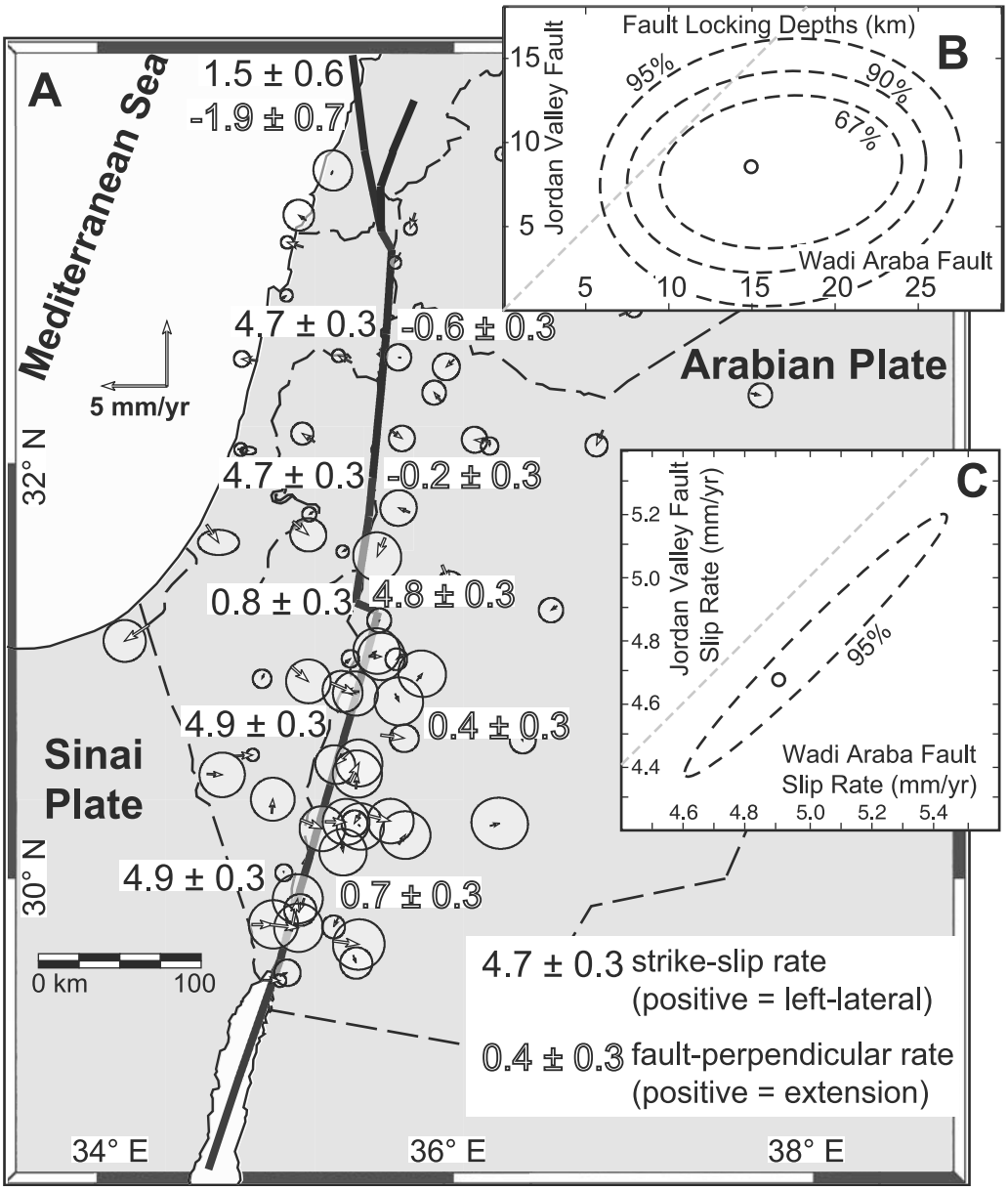

Figure 6. (a) Block model for the southern Dead Sea Fault System showing best fit velocities from the 2-D analysis. (b) Confidence limits on effective depth of fault locking for the Jordan Valley and Wadi Araba faults from block model analysis incorporating noise. Confidence ellipses for 67%, 90%, and 95% are shown. Dashed, gray line denotes equal locking depths. Much of the confidence region is outside of the range of equal fault locking depths. (c) 95% confidence limits on range of fault slip rates for the two fault segments, based on the block model. The strong covariance between the two faults reflects the fact that both faults are linked through their mutual dependency on plate motion. Dashed gray line denotes equal slip rate values.

Wadi Araba Fault. The slip rate magnitudes are slightly greater than, but statistically similar to, slip rates predicted by the regional block model of *Reilinger et al.* [2006] (based primarily on far-field GPS with an assumed locking depth). However, we believe that kinematic modeling of the new results (which include solving for locking depth) is more robust with regard to the DSF owing to the inclusion of near-field data.

[36] On a final note, in the best fitting block model, there are no statistically significant residual velocities (i.e., misfit) that require adding another block boundary (i.e., the Carmel Fault). This does not necessarily discount present-day activity of the

Carmel Fault; in fact, infrequent seismicity suggests some degree of activity [e.g., *Hofstetter et al.*, 1996]. However, the implication is that deformation associated with it is smaller than the detection threshold of GPS, and there is no measurable strain accumulating.

5. Discussion and Tectonic Implications

5.1. Regional Tectonics

[37] The block model from this study incorporates both far-field constraints and near-field constraints. The Euler pole describing the relative motion of the Arabian and Sinai plates is 34.51 ± 3.2°N, 31.25 ± 4.5°E, 0.52 ± 0.045°/yr. We prefer block-model based estimates to other recent estimates of Arabia-Sinai Euler poles based on geologic slip rates [e.g., *Klinger et al.*, 2000a; *Le Beon et al.*, 2010] or 1-D dislocation models [e.g., *Le Beon et al.*, 2008; *Wdowinski et al.*, 2004]; such models are predicated on the assumption that all plate motion is parallel to the transform and, therefore, the southern DSF traces the arc of a great circle about the Euler Pole. In contrast, 2-D models permit plate motion both parallel and orthogonal to boundaries and provide more robust estimation of an Euler pole. In general, far-field locations should provide sufficient control of plate motion, barring internal deformation. Although located slightly farther north and east of the pole of *Reilinger et al.* [2006], the poles overlap considerably within the uncertainties.

[38] The block model also permits revisiting the "leaky" transform hypothesis for the DSF. Some transform-orthogonal extension is suggested for the Wadi Araba section of the DSF, but the best fitting block models suggest no transtension along the Jordan Valley. The small amount of opening along the Wadi Araba Fault (6–17% of the strike-slip rate) is similar to the relative magnitudes of opening and strike-slip used by *Devès et al.* [2011] to model first-order topography along the southern DSF, and by *Smit et al.* [2010] who applied analog modeling to approximate overall basin structure. This suggests that GPS-derived kinematics may reflect the long-term, late Cenozoic behavior of the Dead Sea Fault. This is further supported by recent studies suggest that the Dead Sea basin may have evolved primarily by increasing strike-slip displacement [*Garfunkel and Ben-Avraham*, 2001]. Hence, the leaky (i.e., transtensional) nature of the southern DSF appears to be relatively confined to the Wadi Araba Fault.

[39] Late Quaternary estimates of slip rates published during the past decade vary between 2–6 mm/yr [e.g., *Le Beon et al.*, 2010; *Makovsky et al.*, 2008; *Ferry et al.*, 2007; *Niemi et al.*, 2001; *Klinger et al.*, 2000a]. The slip rates based on elastic modeling of our GPS results are generally consistent with the upper range of these neotectonic estimates. This suggests that the elastic model approximations are probably sufficient to model the GPS velocities along the DSF. Furthermore, if modified, visco-elastic models [e.g., *Savage and Prescott*, 1978] are considered, the congruence of slip rate estimates based on elastic models and geologic estimates implies that the lower crustal viscous relaxation time is greater than the ~1,100 year average recurrence period for the southern DSF. A long relaxation time suggests the possibility of a relatively high viscosity lower crust, which may be consistent with lower crustal seismicity [e.g., *Shamir*, 2006; *Aldersons et al.*, 2003]. The lower crust may be sufficiently viscous that shear remains confined to a relatively narrow zone. Integrated geophysical observations of the southern DSF [*Weber et al.*, 2009] suggest that the transform cuts through the mantle lithosphere as a narrow, subvertical zone. That observation, along with the congruence of elastic models and neotectonic slip rates, are consistent with a 'Deep-Slip' model for interseismic strain accumulation, in which crustal faults are loaded by slip in the lower crust and mantle lithosphere [*Scholz*, 2002].

5.2. Fault Segmentation and Lithospheric Heterogeneity

[40] As noted above, the block model suggests along-strike variation in the effective locking depth along the southern Dead Sea Fault. Although effective locking depth is not necessarily the true depth of fault locking within the crust (the abrupt transition from locking to slipping is not generally realistic), it nonetheless represents the total rate of elastic strain and moment accumulation along a fault. Apparent variations in effective locking depth along the southern DSF may exemplify different seismogenic character of the two major segments. These locking depths also approximate two concentrations in crustal seismicity located by *Shamir* [2006] at 10 and 16 km, respectively. Further, differences in seismic behavior between the WAF and JVF are suggested by assessment of the magnitude-frequency scaling by *Al-Homoud* [2003], who reported b-values of 0.89 and 0.77 for the JVF and WAF, respectively, although confidence limits are not reported from that study.

[41] These apparent seismogenic variations correspond with aforementioned variations in lithospheric structure beneath the DSF. As suggested by studies of regional seismic wave velocities and attenuation [*Bao et al.*, 2011; *Al-Lazki et al.*, 2004; *Al-Damegh et al.*, 2004], the uppermost mantle (i.e., the mantle lithosphere) beneath the JVF and Dead Sea basin may be warmer and/or thinner than the mantle lithosphere beneath the WAF. Additionally, variations in long-term lithospheric strength may also correspond with segmentation of the southern DSF. For example, *Götze et al.* [2007] documented variations in long-term, flexural rigidity (effective elastic thickness) along the southern DSF consistent with inferred seismogenic segmentation. Those authors found weaker elastic lithosphere around the Dead Sea (and areas northward) compared with the Wadi Araba region. Hence, shallower depths of fault locking appear to be associated with warmer mantle lithosphere along the southern DSF.

[42] For comparison with another continental transform, spatial variations in effective locking depth have also been documented along the southern San Andreas Fault, where a systematic analysis of effective locking depths as been recently published by *Smith-Konter et al.* [2011]. An overall trend of decreasing locking depth is observed from the southern San Andreas and San Jacinto faults (locking depths of 16–21 km depth) southward toward the Salton Trough where fault locking is 10–12 km, and shallower, still for the Imperial Valley Fault with 3–9 km locking depths. Although the uncertainties for individual fault segments may be relatively large (e.g., along the San Andreas Fault near Palm Springs), the general southward decrease in effective locking depth appears to be robust. Furthermore, this pattern of locking depth variability is consistent with results from other studies applying block models to analyze interseismic strain in southern California [e.g., *Loveless and Meade*, 2011; *Meade and Hager*, 2005], as well as recent modeling spatial variability of elastic rigidity based on geodetic data [*Chéry et al.*, 2011].

[43] Similar to the DSF, the shallower depths of effective fault locking depths are generally associated with regions of anomalously slow and attenuating mantle lithosphere (i.e., warm and/or thin upper mantle) [e.g., *Buehler and Shearer*, 2010; *Hearn*, 1996; *Lawrence and Prieto*, 2011]. Seismic tomography of P wave and S wave velocities as shallow a 60 km indicate a thinned mantle lid and Vp/Vs ratios suggest partial melt at these depths beneath the shallowest locking depths in the Salton Trough [*Schmandt and Humphreys*, 2010]. In the case of the southern San Andreas Fault, warmer upper mantle (and thinner lithosphere) is related to proto-oceanic rifting at the northern end of the Gulf of California [e.g., *Lachenbruch et al.*, 1985].

[44] The examples of the Dead Sea Fault and San Andreas Fault suggest that thermal structure of the upper most mantle may, in part, influence faulting locking in the upper crust. Thermomechanical models have been applied to relate seismicity to lithospheric structure and thermal state [e.g., *Miller and Furlong*, 1988], and depths of seismicity are often linked to fault locking depths [e.g., *Smith-Konter et al.*, 2011]. In simplified models of crustal strength, the depth of fault locking may generally correspond with the transition from brittle to ductile failure [e.g., *Scholz*, 2002; *Sibson*, 1982]. However, a direct link between lithospheric structure and effective fault locking depth has not been explored, likely due, in part, to broad ranges on the uncertainties in fault locking depths. We suggest that, with improved resolution of effective fault locking depths, such as those reported herein, such a link may be assessed. As discussed by *Miller and Furlong* [1988], spatial variations in seismic behavior can be controlled by thermal state, regional stress magnitude, strain rate, and lithology. The southern DSF is a long-lived (18+ m.y.), lithospheric structure that cuts the entire crust [e.g., *Weber et al.*, 2009]; for such "mature" faults, the primary factor influencing seismicity is generally the thermal state of the lithosphere [e.g., *Miller and Furlong*, 1988]. The thermal structure of the upper mantle beneath the DSF, as imaged seismologically, is consistent with this.

[45] First-order segmentation of the southern DSF corresponds with the Dead Sea basin, a feature that developed with the Middle Miocene initiation of the transform [*Garfunkel and Ben-Avraham*, 2001; *Ben-Avraham et al.*, 2008]. Therefore, segmentation of the southern DSF predates the upper mantle thermal anomaly and is more probably due to factors such as inherited crustal structure [e.g., *Weber et al.*, 2009], rather than a result of the thermal anomaly. Superposition of the present thermal structure, perhaps by a mantle plume onto this segmented transform results in segments with different seismogenic characteristics, as expressed by variation in fault moment accumulation.

6. Conclusions

[46] New GPS measurements from Jordan, combined with other regional data, provide a compre-

hensive view of present-day, near-field deformation associated with the southern Dead Sea Fault (DSF). The results demonstrate that slip rates of 4.4–5.2 mm/yr are conserved between the Wadi Araba and Jordan Valley faults across the Dead Sea basin. Additionally, the GPS velocities suggest minimal extension perpendicular to the transform (i.e., transtension) and suggest that the Carmel Fault does not transfer significant plate motion from the DSF.

[47] The model-derived slip rates are generally consistent with the upper end of recently reported estimates based on offset, Late Quaternary landforms. This consistency of short-term and long-term slip rate estimates suggests that the slip rate has not varied over time. Similarity of GPS-based and long-term slip rates may further suggest that the lower crust has a relatively high viscosity, if modified visco-elastic models of faulting are considered.

[48] Elastic block modeling of GPS velocities suggests along-strike variations in effective fault locking depth along the DSF that correspond with heterogeneity in the mantle lid. Although other factors may be at work, the correlation with uppermost mantle seismic anomalies suggests that, in the case of the southern DSF, first-order variations in seismic moment accumulation may be influenced by the thermal state of the uppermost mantle.

Acknowledgments

[49] The authors acknowledge helpful reviews and feedback from A. Agnon, T. Becker, and an anonymous reviewer. This research acknowledges some logistical support provided by the Hashemite University for field work. Field work during 2005–2009, as well as instrumentation, were supported by grants from the University of Missouri Research Board and the University of Missouri Research Council. The 2010 field survey was supported by NSF grant EAR-0948487. We also acknowledge data services provided by the UNAVCO Facility and SOPAC. Al-Tarazi acknowledges support for sabbatical leave (2010–2011) to Al Bayt University which facilitated some of his efforts. This work was also made possible by assistance with field work and continuous GPS stations provided by Abu Aziz (Aqaba), Ahmed Shreideh (Deir Abi Saeid), Tayel El Hassan (Mutah University), Ahmed Al Amri (JUST), Tahani al Salhi (Petra), Suleiman and Ali (Mua'adi). Field survey assistance: Yasser Al-Shurbaji and Ali El Zeoid (Hashemite Univ.), Tony Bollasina (MU), Tony Nemer (MU), Mahmoud Freihat, and Bjorn Held.

References

Alchalbi, A., et al. (2010), Crustal deformation in northwestern Arabia from GPS measurements in Syria: Slow slip rate along the northern Dead Sea Fault, *Geophys. J. Int.*, *180*, 125–135, doi:10.1111/j.1365-246X.2009.04431.x.

Al-Damegh, K., E. Sandvol, A. Al-Lazki, and M. Barazangi (2004), Regional seismic wave propagation (Lg and Sn) and Pn attenuation in the Arabian Plate and surrounding regions, *Geophys. J. Int.*, *157*, 775–795, doi:10.1111/j.1365-246X.2004.02246.x.

Aldersons, F., Z. Ben-Avraham, A. Hofstetter, E. Kissling, and T. Al-Yazjeen (2003), Lower-crustal strength under the Dead Sea basin from local earthquake data and rheological modeling, *Earth Planet. Sci. Lett.*, *214*, 129–142, doi:10.1016/S0012-821X(03)00381-9.

Al-Homoud, A. S. (2003), Evaluation of strong motion acceleration for embankment dam design considering local seismotectonics, *Nat. Hazards*, *29*, 37–56, doi:10.1023/A:1022929306499.

Al-Lazki, A. I., E. Sandvol, D. Seber, M. Barazangi, N. Turkelli, and R. Mohamad (2004), Pn tomographic imaging of mantle lid velocity and anisotropy at the junction of the Arabian, Eurasian and African plates, *Geophys. J. Int.*, *158*, 1024–1040, doi:10.1111/j.1365-246X.2004.02355.x.

Al-Tarazi, E., E. Sandoval, and F. Gomez (2006), The February 11, 2004 Dead Sea earthquake Ml = 5.2 in Jordan and its tectonic implication, *Tectonophysics*, *422*, 149–158, doi:10.1016/j.tecto.2006.05.010.

Ambraseys, N. N., C. P. Melville, and R. D. Adams (1994), *The Seismicity of Egypt, Arabia, and the Red Sea: A Historical Review*, 181 pp., Cambridge Univ. Press, Cambridge, U. K., doi:10.1017/CBO9780511524912.

Bao, X., et al. (2011), Pg attenuation tomography within the northern Middle East, *Bull. Seismol. Soc. Am.*, *101*(4), 1496–1506, doi:10.1785/0120100316.

Barberi, F., G. Capaldi, P. Gasperini, G. Marinelli, R. Santacroce, R. Scandone, M. Treuil, and J. Varet (1980), Recent basaltic volcanism of Jordan and its implications on the geodynamic history of the Dead Sea shear zone, in *Geodynamic Evolution of the Afro-Arabian Rift System*, edited by A. Carrelli, pp. 667–683, Accad. Naz. dei Lincei, Rome.

Bartov, Y., G. Steinitz, M. Eyal, and Y. Eyal (1980), Sinistral movement along the Gulf of Aqaba–its age and relation to the opening of the Red Sea, *Nature*, *285*, 220–222.

Ben-Avraham, Z., Z. Garfunkel, and M. Lazar (2008), Geology and evolution of the southern Dead Sea Fault with emphasis on subsurface structure, *Annu. Rev. Earth Planet. Sci.*, *36*, 357–387, doi:10.1146/annurev.earth.36.031207.124201.

Buehler, J. S., and P. M. Shearer (2010), Pn tomography of the western United States using USArray, *J. Geophys. Res.*, *115*, B09315, doi:10.1029/2009JB006874.

Camp, V. E., and M. J. Roobol (1989), The Arabian continental alkali basalt province: Part I. Evolution of Harrat Rahat, Kingdom of Saudi Arabia, *Geol. Soc. Am. Bull.*, *101*, 71–95, doi:10.1130/0016-7606(1989)101<0071:TACABP>2.3.CO;2.

Chaimov, T. A., M. Barazangi, D. Al-Saad, T. Sawaf, and A. Gebran (1990), Crustal shortening in the Palmyride fold belt, Syria, and implications for movement along the Dead Sea Fault System, *Tectonics*, *9*(6), 1369–1386, doi:10.1029/TC009i006p01369.

Chang, S.-J., and S. Van der Lee (2011), Mantle plumes and associated flow beneath Arabia and East Africa, *Earth Planet. Sci. Lett.*, *302*, 448–454, doi:10.1016/j.epsl.2010.12.050.

Chéry, J., B. Mohammadi, M. Peyret, and C. Joulain (2011), Plate rigidity inversion in southern California using interseismic

GPS velocity field, *Geophys. J. Int.*, *187*, 783–796, doi:10.1111/j.1365-246X.2011.05192.x.

DeMets, C., R. G. Gordon, D. F. Argus, and S. Stein (1994), Effect of recent revisions to the geomagnetic reversal time scale on estimates of current plate motions, *Geophys. Res. Lett.*, *21*(20), 2191–2194, doi:10.1029/94GL02118.

Devès, M., G. C. P. King, Y. Klinger, and A. Agnon (2011), Localised and distributed deformation in the lithosphere: Modelling the Dead Sea region in 3 dimensions, *Earth Planet. Sci. Lett.*, *308*, 172–184, doi:10.1016/j.epsl.2011.05.044.

Dong, D., T. A. Herring, and R. W. King (1998), Estimating regional deformation from a combination of space and terrestrial geodetic data, *J. Geod.*, *72*, 200–214, doi:10.1007/s001900050161.

Ferry, M., M. Meghraoui, N. A. Karaki, M. Al-Taj, H. Amoush, S. Al-Dhaisat, and M. Barjous (2007), A 48-kyr-long slip rate history for the Jordan Valley segment of the Dead Sea Fault, *Earth Planet. Sci. Lett.*, *260*, 394–406, doi:10.1016/j.epsl.2007.05.049.

Ferry, M., M. Meghraoui, N. Abou Karaki, M. Al-Taj, and L. Khalil (2011), Episodic behavior of the Jordan Valley section of the Dead Sea Fault inferred from a 14-ka-long integrated catalog of large earthquakes, *Bull. Seismol. Soc. Am.*, *101*(1), 39–67, doi:10.1785/0120100097.

Freund, R., Z. Garfunkel, I. Zak, M. Goldberg, T. Weissbrod, and B. Derin (1970), The shear along the Dead Sea rift, *Philos. Trans. R. Soc. London A*, *267*(1181), 107–130, doi:10.1098/rsta.1970.0027.

Garfunkel, Z. (1981), Internal structure of the Dead Sea leaky transform (rift) in relation to plate kinematics, *Tectonophysics*, *80*, 81–108, doi:10.1016/0040-1951(81)90143-8.

Garfunkel, Z. (1989), Tectonic setting of Phanerozoic magmatism in Israel, *Isr. J. Earth Sci.*, *38*, 51–74.

Garfunkel, Z., and Z. Ben-Avraham (2001), Basins along the Dead Sea Transform, in *Peri-Tethyan Rift/Wrench Basins and Passive*, *Peri-Tethys Mem.*, vol. 6, edited by W. C. P. A. Ziegler, A. H. F. Robertson, and S. Crasquin-Soleau, *Mem. Mus. Natl. Hist. Nat.*, *186*, 607–627.

Ginat, H., Y. Enzel, and Y. Avni (1998), Translocated Plio-Pleistocene drainage systems along the Arava fault of the Dead Sea transform, *Tectonophysics*, *284*, 151–160, doi:10.1016/S0040-1951(97)00165-0.

Gomez, F., et al. (2007), Global Positioning System measurements of strain accumulation and slip transfer through the restraining bend along the Dead Sea Fault System in Lebanon, *Geophys. J. Int.*, *168*, 1021–1028, doi:10.1111/j.1365-246X.2006.03328.x.

Götze, H.-J., R. El-Kelani, S. Schmidt, M. Rybakov, M. Hassouneh, H.-J. Forster, and J. Ebbing (2007), Integrated 3D density modelling and segmentation of the Dead Sea Transform, *Int. J. Earth Sci.*, *96*, 289–302, doi:10.1007/s00531-006-0095-5.

Hearn, T. M. (1996), Anisotropic Pn tomography in the western United States, *J. Geophys. Res.*, *101*, 8403–8414, doi:10.1029/96JB00114.

Hempton, M. R. (1987), Constraints on Arabian plate motion and extensional history of the Red Sea, *Tectonics*, *6*(6), 687–705, doi:10.1029/TC006i006p00687.

Herring, T. A., R. W. King, and S. C. McClusky (1997), Geodetic constraints on interseismic, coseismic, and postseismic deformation in southern California, annual report, South. Calif. Earthquake Cent., Los Angeles. [Available at http://www.scec.org/research/98research/98herringetal.pdf.]

Hofstetter, A., T. van Eck, and A. Shapira (1996), Seismic activity along fault branches of the Dead Sea-Jordan Transform System: The Carmel-Tirtza fault system, *Tectonophysics*, *267*, 317–330, doi:10.1016/S0040-1951(96)00108-4.

Ilani, S., Y. Harlavan, K. Tarawneh, I. Rabba, R. Weinberger, K. Ibrahim, S. Peltz, and G. Steinitz (2001), New K-Ar ages of basalts from Harrat Ash Shaam volcanic field in Jordan: Implications for span and duration of upper-mantle upwelling beneath the western Arabian plate, *Geology*, *29*, 171–174, doi:10.1130/0091-7613(2001)029<0171:NKAAOB>2.0.CO;2.

Joffe, S., and Z. Garfunkel (1987), Plate kinematics of the circum Red Sea–A re-evaluation, *Tectonophysics*, *141*, 5–22, doi:10.1016/0040-1951(87)90171-5.

King, R. W., and Y. Bock (1998), *Documentation of MIT GPS Analysis Software: GAMIT*, Mass. Inst. of Technol., Cambridge, Mass.

Klinger, Y., J. P. Avouac, N. Abou Karaki, L. Dorbath, L. Bourles, and J. Reys (2000a), Slip rate on the Dead Sea transform fault in the northern Araba Valley (Jordan), *Geophys. J. Int.*, *142*(3), 755–768, doi:10.1046/j.1365-246x.2000.00165.x.

Klinger, Y., J. P. Avouac, L. Dorbath, N. Abou Karaki, and N. Tisnerat (2000b), Seismic behaviour of the Dead Sea fault along the Araba valley, Jordan, *Geophys. J. Int.*, *142*(3), 769–782, doi:10.1046/j.1365-246x.2000.00166.x.

Lachenbruch, A. H., J. H. Sass, and S. P. Galanais Jr (1985), Heat flow in southernmost California and the origin of the Salton Trough, *J. Geophys. Res.*, *90*, 6709–6736, doi:10.1029/JB090iB08p06709.

Laske, G., M. Weber, and the DESSERT Working Group (2008), Lithosphere structure across the Dead Sea Transform as constrained by Rayleigh waves observed during the DESERT experiment, *Geophys. J. Int.*, *173*, 593–610, doi:10.1111/j.1365-246X.2008.03749.x.

Lawrence, J. F., and G. A. Prieto (2011), Attenuation tomography of the western United States from ambient seismic noise, *J. Geophys. Res.*, *116*, B06302, doi:10.1029/2010JB007836.

Lazar, M., Z. Ben-Avraham, and U. Schattner (2006), Formation of sequential basins along a strike-slip fault–Geophysical observations from the Dead Sea basin, *Tectonophysics*, *421*, 53–69, doi:10.1016/j.tecto.2006.04.007.

Le Beon, M., Y. Klinger, A. Q. Amrat, A. Agnon, L. Dorbath, G. Baer, J.-C. Ruegg, O. Charade, and O. Mayyas (2008), Slip rate and locking depth from GPS profiles across the southern Dead Sea Transform, *J. Geophys. Res.*, *113*, B11403, doi:10.1029/2007JB005280.

Le Beon, M., Y. Klinger, M. Al-Qaryouti, A.-S. Meriaux, R. C. Finkel, A. Elias, O. Mayyas, F. J. Ryerson, and P. Tapponnier (2010), Early Holocene and Late Pleistocene slip rates of hte southern Dead Sea Fault determined from ^{10}Be cosmogenic dating of offset alluvial deposits, *J. Geophys. Res.*, *115*, B11414, doi:10.1029/2009JB007198.

Loveless, J. P., and B. J. Meade (2011), Stress modulation on the San Andreas fault by interseismic fault system interactions, *Geology*, *39*, 1035–1038, doi:10.1130/G32215.1.

Mahmoud, S., R. Reilinger, S. McClusky, P. Vernant, and A. Tealeb (2005), GPS evidence for northward motion of the Sinai block: Implications for E. Mediterranean tectonics, *Earth Planet. Sci. Lett.*, *238*, 217–224, doi:10.1016/j.epsl.2005.06.063.

Makovsky, Y., A. Wunch, R. Ariely, Y. Shaked, A. Rivlin, A. Shemesh, Z. Ben-Avraham, and A. Agnon (2008), Quaternary transform kinematics constrained by sequence stratigraphy and submerged coastline features; the Gulf of Aqaba,

Earth Planet. Sci. Lett., *271*, 109–122, doi:10.1016/j.epsl.2008.03.057.

Mao, A., C. Harrison, and T. Dixon (1999), Noise in GPS coordinate time series, *J. Geophys. Res.*, *104*, 2797–2816, doi:10.1029/1998JB900033.

Marco, S., M. Stein, A. Agnon, and H. Ron (1996), Long-term earthquake clustering: A 50,000-year paleoseismic record in the Dead Sea Graben, *J. Geophys. Res.*, *101*(B3), 6179–6191, doi:10.1029/95JB01587.

McClusky, S., et al. (2000), Global Positioning System constraints on plate kinematics and dynamics in the eastern Mediterranean and Caucasus, *J. Geophys. Res.*, *105*, 5695–5719.

McClusky, S., R. Reilinger, S. Mahmoud, D. B. Sari, and A. Tealeb (2003), GPS constraints on Africa (Nubia) and Arabia plate motions, *Geophys. J. Int.*, *155*, 126–138, doi:10.1046/j.1365-246X.2003.02023.x.

Meade, B. J., and B. H. Hager (2005), Block models of crustal motion in southern California constrained by GPS measurements, *J. Geophys. Res.*, *110*, B03403, doi:10.1029/2004JB003209.

Meade, B. J., and J. P. Loveless (2009), Block modeling with connected fault-network geometries and a linear elastic coupling estimator in spherical coordinates, *Bull. Seismol. Soc. Am.*, *99*, 3124–3139, doi:10.1785/0120090088.

Miller, C. K. and K. P. Furlong (1988), Thermal mechanical controls on seismicity depth distributions in the San Andreas Fault zone, *Geophys. Res. Lett.*, *15*, 1429–1432.

Niemi, T. M., H. Zhang, M. Atallah, and B. J. Harrison (2001), Late Pleistocene and Holocene slip rate of the Northern Wadi Araba fault, Dead Sea Transform, Jordan, *J. Seismol.*, *5*, 449–474, doi:10.1023/A:1011487912054.

Nof, R. N., G. Baer, Y. Eyal, and F. Novali (2007), Recent crustal movements along the Carmel Fault System, Israel, in *EnviSat Symposium 2007* [CD-ROM], *Eur. Space Agency Spec. Publ.*, *ESA SP-636*, 6 pp.

Quennell, A. M. (1984), The Western Arabia rift system, in *Geological Evolution of the Eastern Mediterranean*, edited by J. E. Dixon and A. H. F. Robertson, *Geol. Soc. Spec. Publ.*, *17*, 775–788.

Reilinger, R., et al. (2006), GPS constraints on continental deformation in the Africa-Arabia-Eurasia continental collision zone and implications for the dynamics of plate interactions, *J. Geophys. Res.*, *111*, B05411, doi:10.1029/2005JB004051.

Reinking, J., H. Smit-Philipp, and G. Even-Tzur (2011), Surface deformation along the Carmel Fault System, Israel, *J. Geodyn.*, *52*, doi:10.1016/j.jog.2011.03.004.

Savage, J. C. (2006), Dislocation pileup as a representation of strain accumulation on a strike-slip fault, *J. Geophys. Res.*, *111*, B04405, doi:10.1029/2005JB004021.

Savage, J. C., and R. O. Burford (1973), Geodetic determination of relative plate motion in central California, *J. Geophys. Res.*, *78*, 832–845.

Savage, J. C., and W. H. Prescott (1978), Asthenosphere readjustment and the earthquake cycle, *J. Geophys. Res.*, *83*, 3369–3376, doi:10.1029/JB083iB07p03369.

Schmandt, B., and E. Humphreys (2010), Seismic heterogeneity and small scale convection in the southern California upper mantle, *Geochem. Geophys. Geosyst.*, *11*, Q05004, doi:10.1029/2010GC003042.

Scholz, C. (2002), *The Mechanics of Earthquakes and Faulting*, 2nd ed., 496 pp., Cambridge Univ. Press, Cambridge, U. K.

Shamir, G. (2006), The active structure of the Dead Sea Depression, in *New Frontiers in Dead Sea Paleoenvironmental Research*, edited by Y. Enzel, A. Agnon, and M. Stein, *Spec. Pap. Geol. Soc. Am.*, *401*, 15–32.

Shaw, J. E., J. A. Baker, M. A. Menzies, M. F. Thirlwall, and K. M. Ibrahim (2003), Petrogenesis of the largest intraplate volcanic field in the Arabian Plate (Jordan): A mixed lithosphere-asthenosphere source activated by lithospheric extension, *J. Petrol.*, *44*, 1657–1679, doi:10.1093/petrology/egg052.

Sibson, R. H. (1982), Fault zone models, heat flow, and the depth distribution of earthquakes in the continental crust of the United States, *Bull. Seismol. Soc. Am.*, *72*, 151–163.

Smit, J., J.-P. Brun, S. Cloetingh, and Z. Ben-Avraham (2010), The rift-like structure and asymmetry of the Dead Sea Fault, *Earth Planet. Sci. Lett.*, *290*, 74–82, doi:10.1016/j.epsl.2009.11.060.

Smith-Konter, B., D. Sandwell, and P. Shearer (2011), Locking depths estimated from geodesy and seismology along the San Andreas Fault System: Implications for seismic moment release, *J. Geophys. Res.*, *116*, B06401, doi:10.1029/2010JB008117.

Wdowinski, S., Y. Bock, G. Baer, L. Prawirodirdjo, N. Bechor, S. Naaman, R. Knafo, Y. Forrai, and Y. Melzer (2004), GPS measurements of current crustal movements along the Dead Sea Fault, *J. Geophys. Res.*, *109*, B05403, doi:10.1029/2003JB002640.

Weber, M., et al. (2009), Anatomy of the Dead Sea Transform from lithospheric to microscopic scale, *Rev. Geophys.*, *47*, RG2002, doi:10.1029/2008RG000264.

Westaway, R. (1994), Present-day kinematics of the Middle East and eastern Mediterranean, *J. Geophys. Res.*, *99*(B6), 12,071–12,090, doi:10.1029/94JB00335.

Zhang, J., Y. Bock, H. Johnson, P. Fang, S. Williams, J. Genrich, S. Wdowinski, and J. Behr (1997), Southern California Permanent GPS Geodetic Array: Error analysis of daily position estimates and site velocities, *J. Geophys. Res.*, *102*, 18,035–18,055, doi:10.1029/97JB01380.